Composite Structures 275 (2021) 114440

Contents lists available at ScienceDirect

Composite Structures

journal homepage: www.elsevier.com/locate/compstruct

Adopting traditional image algorithms and deep learning to build the finite model of a 2.5D composite based on X-Ray computed tomography

Yunfa Jia [a,b], Guoqiang Yu [a,b,*], Jinkang Du [a,b], Xiguang Gao [a,b,*], Yingdong Song [a,b,c], Fang Wang [d]

[a] *Key Laboratory of Aero-engine Thermal Environment and Structure, Ministry of Industry and Information Technology, College of Energy and Power Engineering, Nanjing University of Aeronautics and Astronautics, Nanjing 210016, People's Republic of China*

[b] *Jiangsu Province Key Laboratory of Aerospace Power System, College of Energy and Power Engineering, Nanjing University of Aeronautics and Astronautics, Nanjing 210016, People 's Republic of China*

[c] *State Key Laboratory of Mechanics and Control Mechanical Structures, Nanjing University of Aeronautics and Astronautics, Nanjing 210016, People's Republic of China*

[d] *College of Chemical Engineering, Nanjing Forestry University, Nanjing 210016, People's Republic of China*

A R T I C L E I N F O

Keywords:
Fabrics/textiles
Microstructures
Finite element analysis (FEA)
CT analysis

A B S T R A C T

A novel methodology combining traditional image algorithms with deep learning is proposed to accurately classify each pixel of the XCT image of 2.5D woven fabrics with fewer user involvement. For images with symmetrical microstructures, we first extracted the weft and matrix edges separately and then performed curve fitting to obtain the warp edges. The regions enclosed by the warp and weft edges were weft regions, and the areas between two warps were warp regions. Then, threshold segmentation was adopted to achieve pixel classification. For an image with asymmetrical microstructures, a fully convolutional neural network consisting of one encoder and two decoder networks was trained using the symmetry image. Finally, two finite element models of the 2.5D composite were established to predict the linear elastic modulus, one containing all the geometries and the other containing only the symmetrical geometry. The results show that the former prediction fit the experimental results better.

1. Introduction

Carbon fiber-reinforced silicon carbide matrix composites (C/SiC composites) are high-performance ceramic matrix composites (CMCs) with excellent properties, such as low density, high temperature resistance, and high strength, and they are considered to be one of the most promising candidate materials for hot end parts of aero engines. In engineering applications, CMC structures are generally woven [12]. Therefore, accurate prediction of the mechanical properties of woven composites is of great practical significance. 2.5D woven fabric is a novel weaving technology that is an improvement over traditional 2D woven fabric. The warp and weft are intertwined to interlock, and the fiber bundles are interwoven through a certain angle in the thickness direction [3], which results in a better anti-delamination performance than 2D and is easier to prepare than 3D woven material.

Currently, the macro-mechanical method treats the composite as anisotropically homogeneous through homogenization, but it cannot reflect the effect of the microstructures on the macro-mechanical response of the composite [1,4,5]. Therefore, it is necessary to adopt a micromechanical method to analyze the composite performance. The establishment of a finite element (FE) model in the micromechanical method includes the following: 1) an idealized representative volume element (RVE) model. By measuring some major geometrical parameters of the 2.5D composite, simplifying and assuming the real microstructures, a smallest periodic RVE model is then established [3,6,7]. Although the entire modeling and analysis process is relatively simple, it does not consider imperfections such as fiber deformation and random pore distribution during the preparation process. 2) Real geometry modeling based on X-ray computed tomography (XCT), it is a nondestructive testing method that can obtain a series of images containing information on the internal microstructures without destroying the composite. These images are segmented by traditional image algorithms and then transformed into a 3D model to build an FE model. Studies have shown that an FE model based on XCT can truly reflect the microstructures of the reinforcement [8,26] or composite [9], and thus the mechanical properties prediction results are closer to the experimental results.

* Corresponding authors at: Key Laboratory of Aero-engine Thermal Environment and Structure, Ministry of Industry and Information Technology, College of Energy and Power Engineering, Nanjing University of Aeronautics and Astronautics, Nanjing 210016, People's Republic of China

E-mail addresses: ygq@nuaa.edu.cn (G. Yu), gaoxiguang@nuaa.edu.cn (X. Gao).

https://doi.org/10.1016/j.compstruct.2021.114440
Received 12 April 2021; Revised 19 July 2021; Accepted 29 July 2021
Available online 31 July 2021

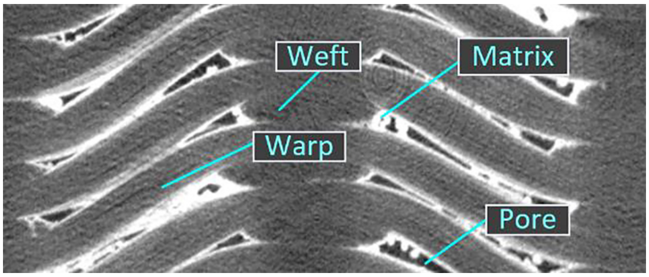

Fig. 1. XCT slice with a symmetrical structure.

Some segmentation methods based on traditional computer vision for XCT slices have been proposed, including multiple types of composites, such as structure tensor for 2D woven textile fabrics [10,28,29], gray-level co-occurrence matrix for 3D orthogonal woven fabrics [8], and fiber-tracking algorithms for multidirectional [+45/90/45/0] carbon fiber-reinforced polymer (CFRP) specimens [11]. These methods are designed according to the characteristics of the *meso*-structure. In addition, the structure tensor and gray-level co-occurrence matrix algorithms depend heavily on the scanning resolution; therefore, they cannot be applied to 2.5D woven fabrics. Considering the fabric compaction and the axial yarn torsion, Liu [30] reconstructed the representative volume element of 3D five-directional braided composites based on a statistical approach. However, this method does not take into account the defects in the matrix preparation process. Gao [12] treated each matrix as a twisted quadrilateral. By searching for a new matrix pixel within the radius *R* of the current matrix pixel, labeling and matching the matrix, the area between adjacent matrices in the vertical direction is the warp. This method requires more manual participation in the process of matrix pairing and the extraction of matrix edges. In addition, some warp directions are different; therefore, it is also necessary to achieve segmentation of individual fiber bundles.

XCT slices of 2.5D woven fabrics include not only symmetrical but also asymmetrical microstructures caused by the manufacturing process, as shown in Fig. 1 and Fig. 12, respectively. However, none of the existing methods considers asymmetric image identification. At present, fully convolutional neural networks (FCNs) [13] have gained wide attention in the field of image segmentation, such as U-net [14] for biological images and SegNet [15] for road traffic. However, there are few articles on methods for fiber-reinforced composites.

Ali [10] and Emerson [16] implemented supervised learning to segment XCT slices; this method required training using XCT slices and corresponding label images. Compared with conventional machine learning algorithms, the deep convolutional neural network (DCNN) showed superior segmentation preference. The size of the training dataset had a strong effect on preference. However, the label images used in these studies were all manually prepared. Data augmentation, which could expand the dataset and significantly improve prediction accuracy, was also not adopted. In addition, various existing neural networks have been designed for relatively complex application scenarios, with many types of classifications and a large number of parameters. However, there are only four categories of 2.5D woven fabrics.

The aim of this work was to 1) adopt traditional computer vision methods to segment images with symmetrical structures; 2) train the multi-decoder network proposed using XCT images with symmetrical structures and study the influence of data augmentation and the number of iterations on segmentation accuracy; and 3) establish two FE models to predict the linear elastic modulus to determine the effect of the microstructures on prediction accuracy.

2. Material and experiment

The carbon fiber was T700-6K (average diameter = 6 μm). The composite was a 2.5D C/SiC woven fabric provided by the Institute of Metal Research, Chinese Academy of Sciences. The volume fractions of the fiber were approximately 43%. The matrix and PyC interface were successively prepared by the chemical vapor infiltration (CVI) process.

An area of 10 mm × 10 mm × 4 mm was cut from the rectangular woven plate using a diamond wire saw. The specimen was scanned using a (Comet, Switzerland) to obtain a series of XCT images containing the internal microstructures of the material. The scanning parameters are presented in Table 1.

The water jet method was used to cut three cuboid-shaped specimens with dimensions of 120 mm × 8 mm × 4 mm, and a uniaxial tensile test was performed on a WDW-100 universal testing machine (Shijin, China). The axial linear elastic modulus of the specimen was 121 GPa according to experiment. The mechanical parameters of the fiber bundle obtained by the mixture method [23] are listed in Table 2, where 1 represents the warp direction of the material, 2 represents the weft direction, and 3 represents the direction perpendicular to 1 and 2. The main elastic parameters of the fiber and matrix can be found in Ref. [24].

3. Image segmentation through traditional image processing

In the XCT images with symmetrical microstructures, the matrix was symmetric on both the left and the right. To facilitate image processing, we first extracted the edges of the matrix of the image and matched them by the center coordinate. Because the edges of the weft and matrix partly overlapped, we selected the weft edges by image gradient and deleted them. The remaining matrix edges were fitted using the least squares method to obtain the complete warp edges; the regions between two matrixes were warp yarn. The regions enclosed by the warp and weft edges were weft regions, as shown in Fig. 1. Finally, the other pixels were classified by threshold segmentation. All these processes were executed in OpenCV.

Table 1
CT parameters used for the composite.

Voltage (Kv)	Power (W)	Projection Number	Exposure Time (s)	Pixel Size (μm)	Width (pixels)	Height (pixels)
60	5	2001	2	11.847	1024	1004

Table 2
Mechanical parameters of fiber bundle (GPa).

E_1	E_2	G_{12}	G_{23}	μ_{23}	μ_{12}
218.8	29.3	26.88	25.7	0.34	0.13

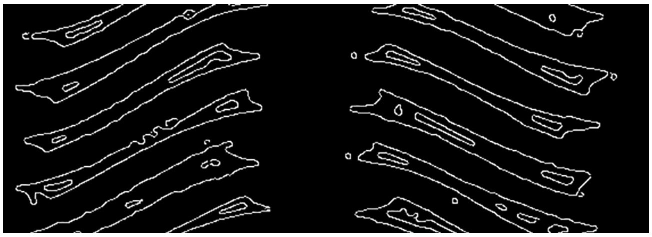

Fig. 2. The edge extracted by the Canny algorithm.

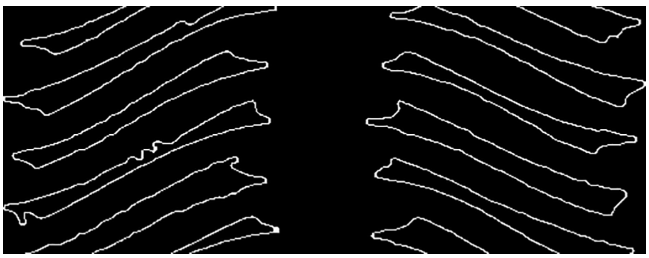

Fig. 3. Regions deleted of pores or noise.

3.1. Matrix pairing

Owing to the obvious difference between the matrix and other components in the slice, the threshold value of the matrix was set to 0.1133 according to threshold selection method proposed by Otsu [27]. Fig. 2 shows the edges extracted by the Canny operator after inverting the resulting image. The image was labeled by eight connected regions, and then the area of the region less than 280 was deleted, as shown in Fig. 3. We checked whether the matrix edges were closed; if not, we performed the inflation operation. The eight connected regions were added again to label every single matrix, and the center coordinates of every matrix were computed. The small yellow triangle shown in Fig. 4(b) represents the center. According to the center coordinate, we judged whether the matrix was located at the same horizontal position, and according to the abscissa, we determined whether the matrix edge was located at the left or the right side to realize matrix pairing.

In addition, the Harris corner detection algorithm was adopted to obtain the corner points, and the top 300 points were selected, marking them with a green cross, as shown in Fig. 4(a). The red dots in Fig. 4(b) show the corner points whose horizontal and vertical coordinate distances are all more than 10 pixels among the 300 corner points. These points were used as described in Section 3.3 to correct the fitting warp edge.

3.2. Weft edge recognition

To obtain the complete warp edges by fitting the matrix edges, weft edges should be removed from the matrix edge. The image itself is a two-dimensional function with a size of $[row, col]$. Therefore, the column gradient of each pixel is

$$I_y = \frac{[f(i,j+1) - f(i,j)]}{2} \tag{1}$$

and the row gradient of each pixel is

$$I_y = \frac{[f(i+1,j) - f(i,j)]}{2} \tag{2}$$

where i and j refer to the rows and columns of the image, respectively. The gradient of each pixel is

$$I_{xy} = I_x. \times I_y \tag{3}$$

Because of the distinct difference in the direction of the warp and weft, the symbol I_{xy} should be opposite in each direction. The number of warp pixels was larger than that of the weft. Therefore, a pixel with a smaller number was considered as the weft edge, and its pixel value was set to 0. The results of a pair of matrix edges are shown in Fig. 5(a) and (b), respectively.

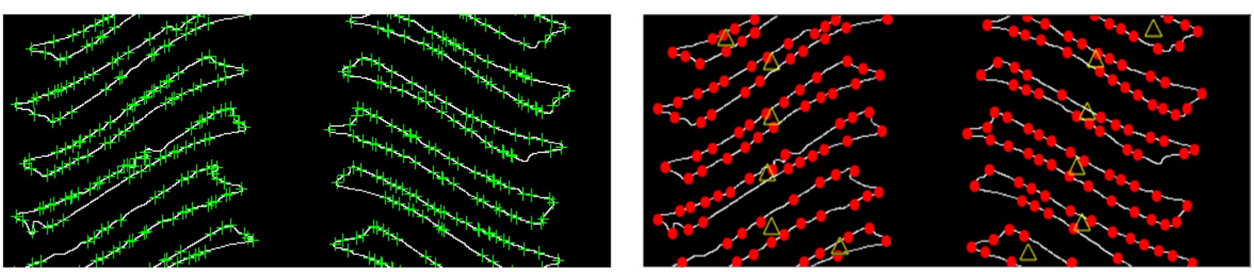

(a) (b)

Fig. 4. (a) Harris corner points. (b) Red dots representing the screened corner points and yellow triangles representing the center of the matrix edges. (For interpretation of the references to color in this figure legend, the reader is referred to the web version of this article.) (For interpretation of the references to color in this figure legend, the reader is referred to the web version of this article.)

(a) (b)

Fig. 5. (a) Left and (b) right matrix edge.

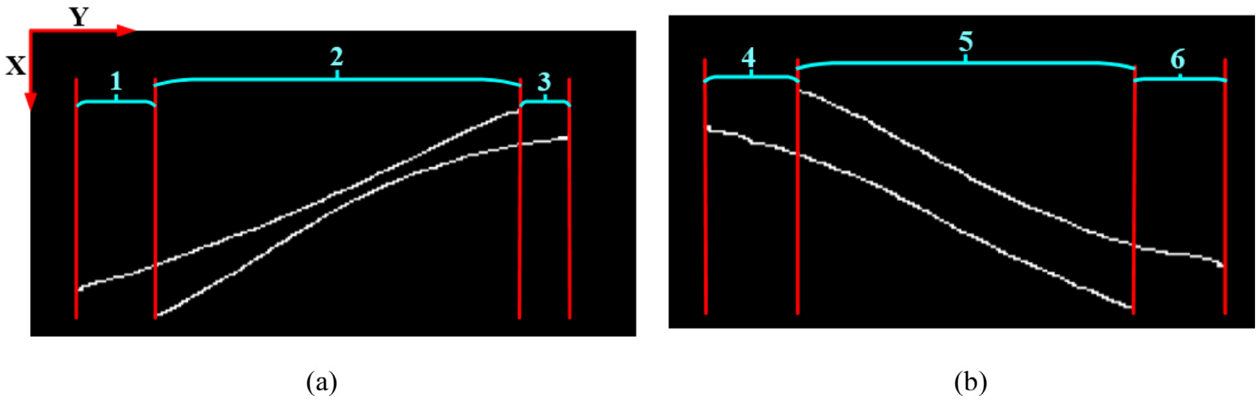

Fig. 6. (a) Left and (b) right edges divided into three parts.

3.3. Extracting upper and lower edge of warp

Fig. 6(a) and (b) show that the matrix edge was divided into three parts based on the number of edge pixels in each column of the image. Areas 1, 3, 2 or 6, 4, 5, contained the upper, lower and upper and lower edges of the matrix, respectively.

The minimum $y_{\min}$ and maximum $y_{\max}$ values of the column coordinates of the left warp edge are shown in Fig. 6(a). The column coordinates of Area 1 ranged from $y_{\min}$ to $(y_{\min}+y_{\max})/2$ and those of Area 3 ranged from $(y_{\min}+y_{\max})/2$ to $y_{\max}$. Within this range, we determined whether the number of column coordinates corresponding to the row coordinate with a pixel value of 1 was 1; if so, they were added to *ext_1* and *ext_2*, which represented the number of coordinates of Areas 1 and 3, respectively, and they were recorded to the coordinate matrix of *coor_ext_1* and *coor_ext_2*.

The column coordinates of Area 2 ranged from $y_{\min}$ to $y_{\max}$. The warp upper and lower edges were recorded as *up_warp* and *down_warp*, respectively. The number of row coordinates, *Row_sim_num*, was counted with the same column coordinates and the row coordinates were recorded as *Coor_coin*. If

$$Coor\_coin(Row\_sim\_num, 1) - Coor\_coin(1,1) \geqslant 3 \tag{4}$$

the row coordinate $Coor\_coin(1)$ and the corresponding column coordinate y were included in *up_warp* and the row coordinate $Coor\_coin(Row\_sim\_num)$ and the corresponding column coordinate y were included in *down_warp*.

Next, the four parts of the matrix edge, the upper and lower edges in Area 2, and two separate small edges in other areas were extracted. The two small edges were then connected to the upper or lower edge of the warp to obtain a complete warp edge.

Comparing Dis_1 with Dis_2, if the former was greater than the latter, then *coor_ext_1* would be given as*down_warp*; otherwise, it would be given as *up_warp*. For *ext_2*, the same comparison was made, and it was connected to the upper or lower edges of the warp edge.

$$Dis_1 = coor\_ext\_1(ext\_1, 1) - up\_warp(1,1) \tag{5}$$

$$Dis_2 = coor\_ext\_1(ext\_1, 1) - down\_warp(1,1) \tag{6}$$

3.4. Edge fitting

To ensure the accuracy of the fitting of the warp edge, the warp upper edge was mirrored symmetrically, and the mirror length was $col/3$. The upper edge of the warp after mirroring was fitted using the least squares method, and the warp trend was obtained. The fitting result is shown in Fig. 7. The extracted Harris corner points were substituted into the corresponding curve function, and then we checked whether the corner points, obtained as described in Section 3.1, were on the curve; if not, the function parameters were fine-tuned. A similar operation was then performed on the lower edge of the warp. These curves were then substituted into the original slice. Fig. 8 shows the fitting edges of the warp after substituting these curves into the original slice. The regions between the two warp curves were warp yarn.

The regions where the image gradient, I_{xy}, calculated as described in Section 3.2, was less than zero were the left edges of the weft; otherwise, they were the right edges. The regions enclosed by the warp and weft edges were the weft yarn. Because the pixel gray values of the matrix and the pores were quite different, they were identified by threshold segmentation. Additionally, we obtained a separate warp area based on the locations of the fitting function, and the final classification image is shown in Fig. 8(b). Then, the skeleton of each warp yarn was extracted to determine the fiber-bundle orientation [25].

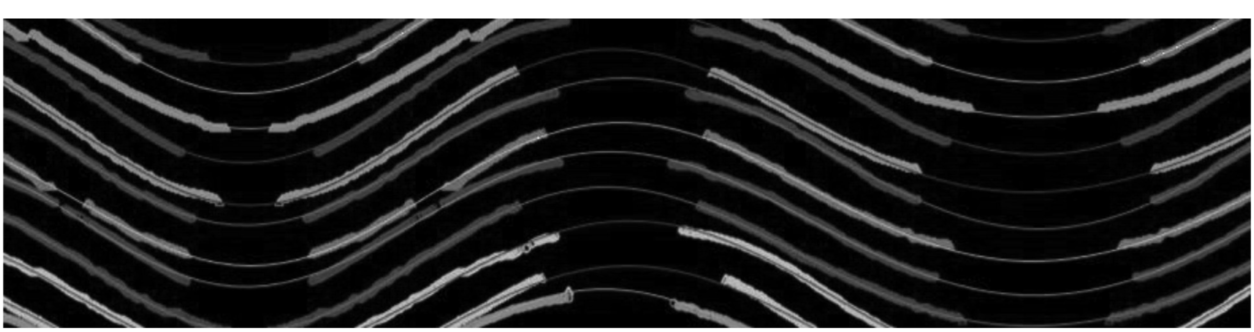

Fig. 7. The fitting result after mirroring the matrix edge.

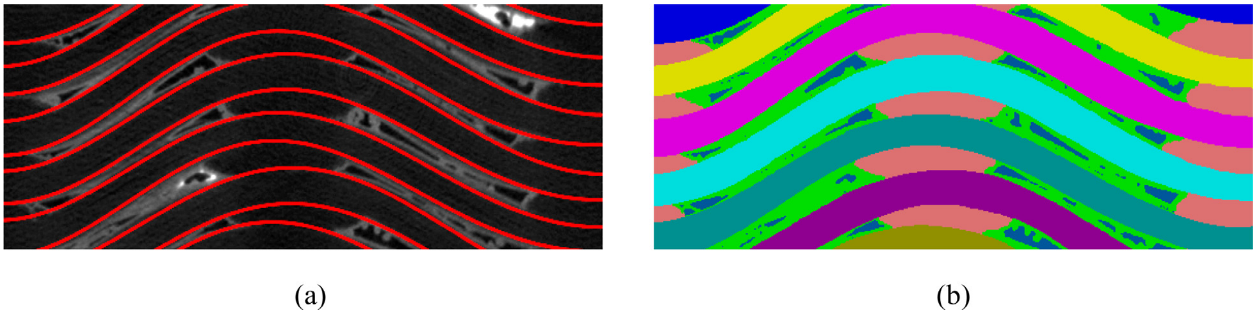

Fig. 8. (a) Substitution of the fitting curve into the original XCT slice. (b) The final result. (For interpretation of the references to color in this figure legend, the reader is referred to the web version of this article.)

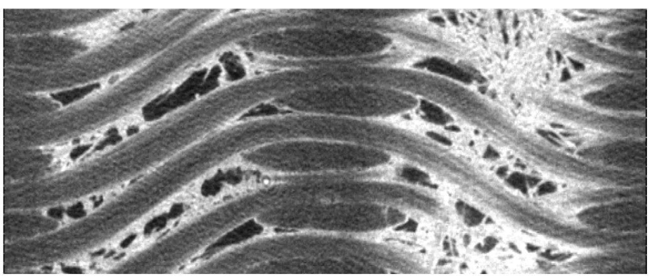

Fig. 9. XCT slices with asymmetrical structure.

3.5. Image segmentation by neural network

The above method provides good classification for XCT slices with symmetric structures. However, it cannot be used for some XCT images where the symmetry is not obvious because the matrix conceals the fiber bundle or because of changes in the yarn direction in the transition zone, as shown in Fig. 9. Currently, such images can only be labeled manually; however, this workload is large. In addition, if they are not labeled by different markers, they may incorporate subjective factors during classification, leading to inaccurate classification.

We propose adopting a fully convolutional neural network (FCN) based on deep learning to identify this type of image, which has received significant attention in image segmentation.

3.6. Database

As described in Section 3, a total of 652 XCT slices were identified. The original XCT slices and the corresponding results were used to establish the database Q for training the FCN. However, owing to separate numbering of the warp, as described in Section 3.4, it is difficult to segment the image using FCN. Therefore, we set all warps to the same pixel value. Fig. 10(a) shows the original XCT image and Fig. 10(b) represents the corresponding labels. In this study, we first divided these images into training set Q1 and testing set Q2, which included 452 and 200 pairs of images, respectively. Random data transforms, including rotation, contrast, and brightness, were adopted to augment training set Q1. There were 1808 pairs of images in Q1. We used the pre- and post-augmentation databases to train the neural network and tested its performance to determine the benefit of data augmentation.

3.7. Network architecture

Fig. 11 shows the established FCN architecture, named the multi-decoder network, which included one encoder and two decoder networks. The encoder network was composed of four encoders and a single convolution layer. Each encoder contained two convolutional layers with a filter size of 3 × 3 and a max-pooling layer with a pooling kernel size of 2 × 2. Each convolutional layer followed a batch normalization (BN) [17] and a ReLU [19] non-linearity [max(0, x)] layer. The configurations of the two convolution layers were the same. However, the feature channels of the second convolutional layer were input to the pooling layer and a 1 × 1 convolutional layer, respectively. The former was used to halve the size of the feature channels, and the latter was used to compress the number of feature channels to reduce the training parameters. When pooling was performed, the indices of the maximum feature value in each pooling kernel were recorded and passed to the up-sampling layer of the decoder. After the fourth encoder was a single convolutional layer with a filter size of 3 × 3. The number of feature channels produced by the convolutional layer of each encoder is listed in Table 3.

The feature channels produced by the last convolutional layer of the encoder network were the input max-pooling index decoder network and the concatenation decoder network. Both were composed of four decoders. The max-pooling index layer was proposed by SegNet [23]; however, this operation may lose some edge information, so that

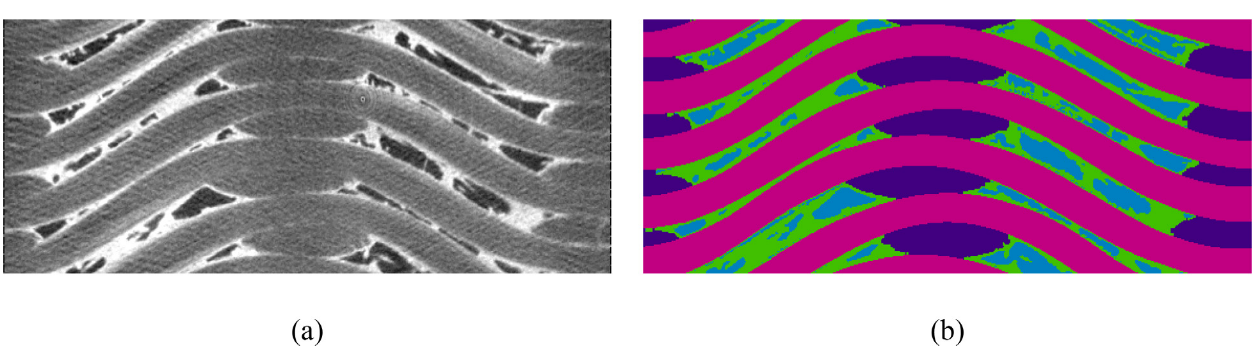

Fig. 10. (a) The original XCT image and (b) the corresponding label image with the same warp pixel values.

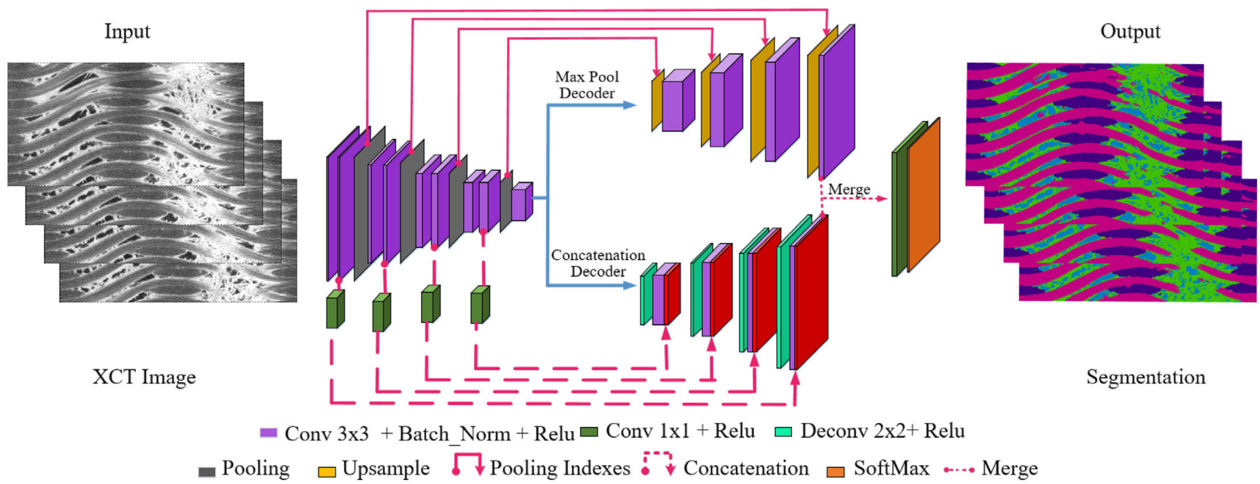

Fig. 11. Architecture of the multi-decoder network. (For interpretation of the references to color in this figure legend, the reader is referred to the web version of this article.)

Table 3
Number of feature channels of the convolution layer of each encoder.

Encoder Network	1	2	3	4	Conv
Feature Channel	32	64	128	256	512

the boundary of each structure is blurred. Therefore, we added the concatenation layer in the FCN to further strengthen the relationship between the shallow and deep networks.

Each max-pooling decoder comprised an up-sampling and a convolutional layer, followed by a BN and ReLU layer. The up-sampling layer was used to double the size of the feature channel, and the maximum feature value index and the value recorded were assigned to the corresponding locations of the feature channel of the up-sampling layer. The convolutional layer was used to further extract the deep semantic information of the image and halve the number of feature channels. Each channel concatenation decoder was composed of a deconvolution layer followed by a ReLU layer, a channel concatenation layer, and a convolution layer followed by a BN and ReLU layer. The output of the deconvolution layer and the corresponding encoder 1×1 convolution layer were concatenated, and then the convolution calculation was performed.

In the fourth decoder, the output of the last convolutional layer of the two decoder networks was merged, and a 1×1 convolutional layer followed by a ReLU layer was used to compress the number of feature channels, the number of which was the same as the number of classifications of the structure, which was four. During training, we used cross-entropy loss [13] as the objective function to train the network. When testing, the merged feature channels were provided to a multi-class soft-max classifier to predict the class probabilities of each pixel independently, and the class of each pixel was the class with the maximum probability.

The number of feature channels of the max-pooling and channel concatenation decoder networks are listed in Tables 4 and 5, respectively.

We adopted the Adam optimizer [20] to train the multi-decoder network with a fixed learning rate of 0.01 and momentum of 0.999; it was implemented using the Caffe framework [18] on a Nvidia RTX 2080 graphics card. The initialization methods for the weight and bias of the convolutional layer used MSRA [19] and a constant, respectively. The number of training iterations was 30,000, and the weight file was saved every 5000 iterations.

Table 4
Number of feature channels of the max-pooling decoder network.

Decoder Network_1	1	2	3	4
Feature Channel	256	128	64	32

3.8. Segmentation results

After the training was completed, each saved weight file was used to segment the XCT slices in the test set separately, and the performance of the network was evaluated through intersection over union (IoU) for each structure and mean intersection over union (MIoU) for all structures.

$$IoU = \frac{p_{ii}}{\sum_{j=0}^{k} p_{ij} + \sum_{j=0}^{k} p_{ji} - p_{ii}} \tag{7}$$

$$MIoU = \frac{1}{k+1} \sum_{i=0} \frac{p_{ii}}{\sum_{j=0}^{k} p_{ij} + \sum_{j=0}^{k} p_{ji} - p_{ii}} \tag{8}$$

Table 5
Number of feature channels of the channel concatenation decoder network.

Decoder Network_2	1		2		3		4	
Layer	Deconv	Conv	Deconv	Conv	Deconv	Conv	Deconv	Conv
Feature Channel	128	128 + 128	128	64 + 64	64	32 + 32	32	16 + 16

Table 6
IoU of each structure and MIoU varying with the iteration before data augmentation.

Iteration	Pore (%)	Matrix (%)	Warp (%)	Weft (%)	MIoU (%)
5000	78.67	74.6	80.5	50.1	70.97
10,000	84.56	78.5	82.21	54.21	74.87
15,000	84.92	78.07	82.18	54.84	75.00
20,000	84.1	77.82	81.29	52.98	74.05
25,000	84.17	77.76	81.38	53.45	74.19
30,000	83.84	77.36	81.38	53.65	74.06

Table 7
The IoU of each structure and MIoU varying with the iteration after data augmentation.

Iteration	Pore (%)	Matrix (%)	Warp (%)	Weft (%)	MIoU (%)
5000	80.56	73.2	85.5	75.2	78.62
10,000	86.81	77.03	90.13	79.64	83.4
15,000	86.62	76.92	89.64	78.56	82.94
20,000	86.7	76.8	89.68	78.52	82.93
25,000	86.74	77.01	89.77	78.46	83.00
30,000	86.5	76.74	89.73	78.29	82.82

where p_{ii} is the number of pixels predicted correctly, k represents the total number of classes included in the slice, p_{ij} means that misclassified the pixels of ith class into jth class, p_{ji} means that misclassified the pixels of jth class into ith class.

Tables 6 and 7 show the changes in IoU and MIoU, respectively, with the number of iterations before and after data augmentation. It is noticeable that data augmentation had a significant effect on the classification results. Before augmentation, the highest MIoU appeared when the number of iterations was 15,000, after which it appeared at 10,000 iterations. At 10,000 times, the MIoU of the latter was approximately 8% higher than that of the former, and the IoU of the weft increased by approximately 25%. In addition, regardless of whether data augmentation was performed, MIoU initially increased and then decreased, which meant that the greater the number of training iterations, the better the prediction result. The classification results of the matrix and the weft were both the worst. On the one hand, because the weft and warp were both carbon fiber bundles, it was difficult to distinguish between them. On the other hand, because the matrix was at the junction of warp yarns and pores, there may have been some regions where the matrix was incorrectly classified, as described in Section 3.

Among the predictions on the test set, the iteration with the highest MIoU was selected to identify the XCT slices with asymmetric structures. Fig. 12 shows the predictions of 10,000 iterations after augmentation. It is worth noting that the neural network could accurately identify these XCT images. Although there were still some classification errors, this process can be used normally with only a few manual corrections. Then, each warp was numbered, and the fiber orientation was determined manually. Correcting errors and warp number can also be performed by traditional image-processing algorithms instead of manual operation if the number of images is relatively large.

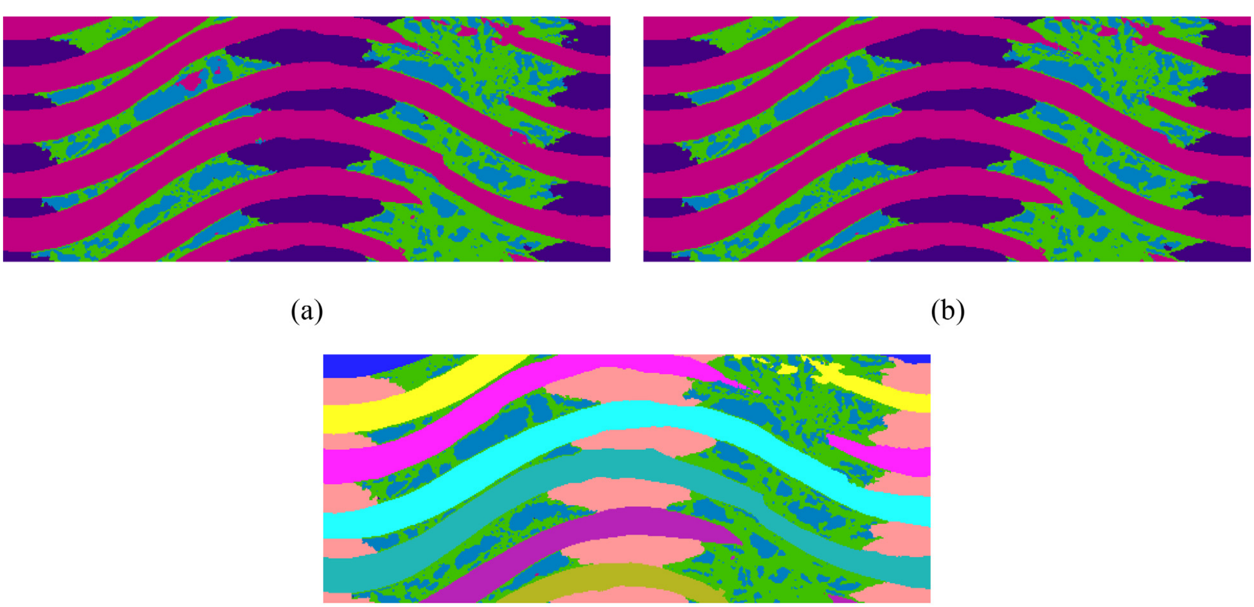

(a) (b) (c)

Fig. 12. (a) The result of image segmented by FCN, (b) the manually corrected results, and (c) the manual warp numbering.

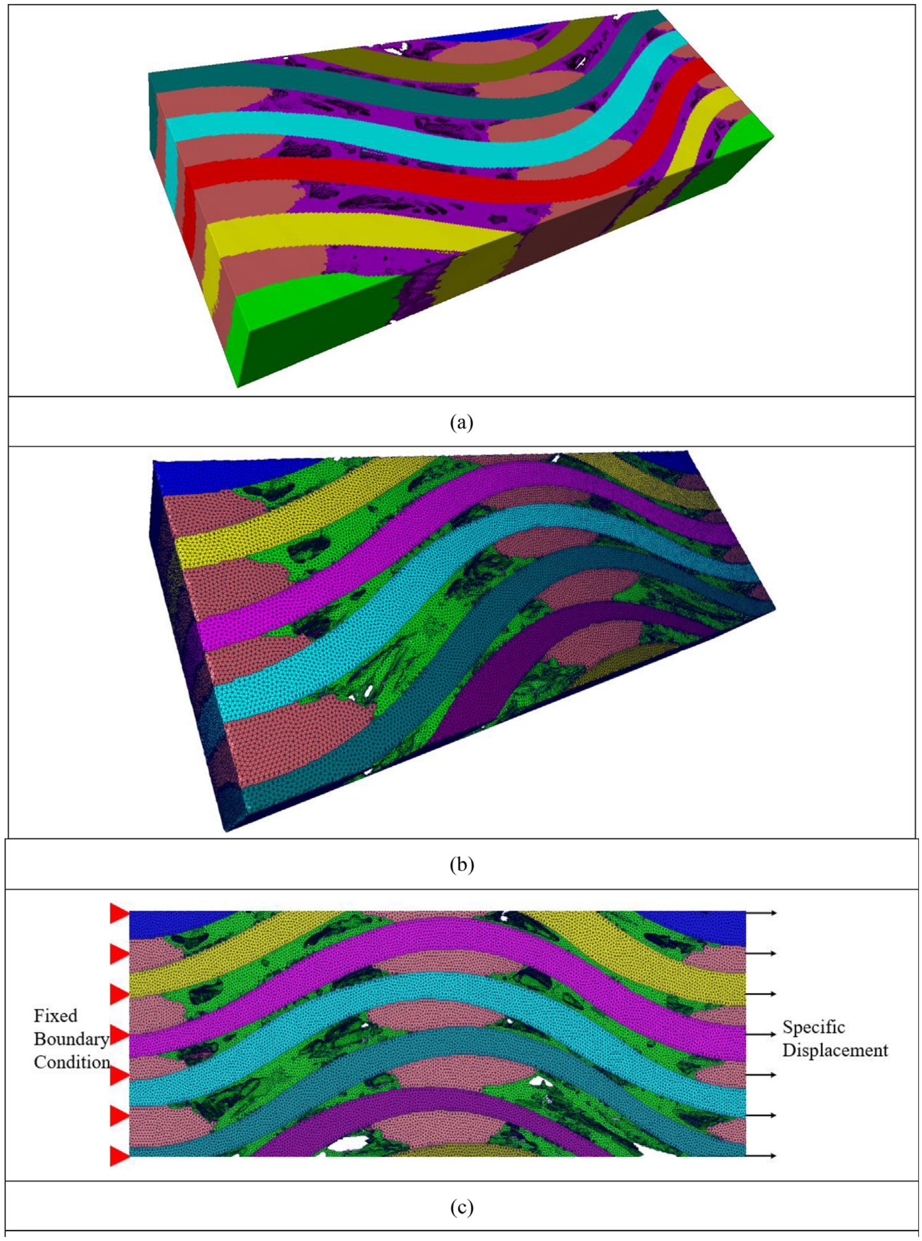

Fig. 13. (a) 3D model reconstructed; (b) FE model; (c) the boundary condition imposed.

4. Model validation

The 3D model of the 2.5D woven fabric composite structure was reconstructed through the marching cube [21] algorithm, and the surface simplification [22] method was adopted to remove the redundant surface. Fig. 13(a) shows the reconstructed 3D model. These were then combined with the advancing-front technique to generate an FE model with tetrahedral mesh, as shown in Fig. 13(b), called the real FE model; the mechanical parameters of the yarn are shown in Table 2. One end of the FE model was fixed, and displacement constraints were applied within the linear elastic range to the other end to simulate the loading process of the uniaxial tensile test, the boundary condition is shown in Fig. 13 (c). Table 8 shows the prediction results for the linear elastic modulus of the composite in the tensile direction. The prediction of the real FE model had better agreement with the experimental results, but it underestimated the performance owing to the complex distribution of the matrix and pores in the transition region matrix. In contrast, the prediction of the perfect FE model overestimated the performance, which was due to the relatively perfect microstructures.

Table 8
Comparison between prediction and experiment.

Results	E_{11}/GPa (Real Model)
Prediction	116
Experiment	121
Error (%)	4.13

5. Conclusions

According to the XCT image features of the 2.5D woven composite such as the symmetry of the internal microstructures, the pixel gray level, and the gradient, a traditional image-processing algorithm was adopted to realize the classification of each pixel in the image. The proposed multi-decoder FCN was trained using the classification results of XCT images with regular microstructures, and then segmentation of images with relatively complex and chaotic internal microstructures was realized. This shows that applying these two methods simultaneously to segment XCT images can greatly save manpower and improve the accuracy of classification. It is worth noting that the training number of the neural network should be up to the point, and the data augmentation had a significant effect on the improvement of accuracy. This study proves once again that the FE model based on XCT images needs to include all the periodic structures of a material to improve the prediction accuracy.

CRediT authorship contribution statement

Yunfa Jia: Conceptualization, Methodology, Investigation, Writing - original draft. **Guoqiang Yu:** Methodology, Writing - review & editing. **Jinkang Du:** Investigation. **Xiguang Gao:** Validation, Writing - review & editing. **Yingdong Song:** Supervision, Validation, Writing - review & editing. **Fang Wang:** Writing - review & editing.

Declaration of Competing Interest

The authors declare that they have no known competing financial interests or personal relationships that could have appeared to influence the work reported in this paper.

Acknowledgement

This work was supported by the National Science and Technology Major Project [grant number 2017-IV-0005-0042].

References

[1] Gao X, Yu G, Xue J, Song Y. Failure analysis of C/SiC composites plate with a hole by the PFA and DIC method. CERAM INT. 2017;43(6):5255-66.
[2] Misra AK, Greenbauer-Seng LA. Aerospace propulsion and power materials and structures research at NASA Glenn Research Center. J Aerospace Eng. 2013;26 (2):459–90.
[3] Lu Z, Zhou Y, Yang Z, Liu Q. Multi-scale finite element analysis of 2.5D woven fabric composites under on-axis and off-axis tension. COMP MATER SCI. 2013;79 (485-94.
[4] Xiguang G, Long Li, Yingdong S. A temperature-dependent constitutive model for fiber-reinforced ceramic matrix composites and structural stress analysis. Int J Damage Mech 2014;23(4):507–22.
[5] Marcin L, Maire J-F, Carrère N, Martin E. Development of a macroscopic damage model for woven ceramic matrix composites. Int J Damage Mech 2011;20 (6):939–57.
[6] Ma J, Xu Y, Zhang L, Cheng L, Nie J, Dong N. Microstructure characterization and tensile behavior of 2.5D C/SiC composites fabricated by chemical vapor infiltration.SCRIPTA MATER.2006;54(11):1967-71.
[7] Chen L, Yao X, Cen S.Predictions of elastic property on 2.5D C/SiC composites based on numerical modeling and semi-analytical method. Composites Part B: Engineering.2015;74(53-65.
[8] Naouar N, Vidal-Salle E, Schneider J, Maire E, Boisse P.3D composite reinforcement meso F.E. analyses based on X-ray computed tomography. COMPOS STRUCT.2015;132:1094-104.
[9] Ali J, Farooqi JK, Buckthorpe D, Cheyne A, Mummery P. Comparative study of predictive FE methods for mechanical properties of nuclear composites. J NUCL MATER. 2009;383(3):247-53.
[10] Wijaya W, Ali MA, Umer R, Khan KA, Kelly PA, Bickerton S. An automatic methodology to CT-scans of 2D woven textile fabrics to structured finite element and voxel meshes. Compos A Appl Sci Manuf 2019;125:105561.
[11] Sencu RM, Yang Z, Wang YC, Withers PJ, Rau C, Parson A, et al. Generation of micro-scale finite element models from synchrotron X-ray CT images for multidirectional carbon fibre reinforced composites. Compos A Appl Sci Manuf 2016;91:85–95.
[12] Gao X, Han X, Song Y.X-ray computed tomography based microstructure reconstruction and numerical estimation of thermal conductivity of 2.5D ceramic matrix composite. CERAM INT.2017;43(13):9790-7.
[13] Long J, Shelhamer E, Darrell T. Fully convolutional networks for semantic segmentation. In: Proceedings of the IEEE Conference on Computer Vision and Pattern Recognition. p. 3431–40.
[14] Ronneberger O, Fischer P, Brox T. U-Net: Convolutional Networks for Biomedical Image Segmentation. In: International Conference on Medical Image Computing and Computer-Assisted Intervention. p. 234–41.
[15] Badrinarayanan Vijay, Kendall Alex, Cipolla Roberto. SegNet: a deep convolutional encoder-decoder architecture for image segmentation. IEEE Trans Pattern Anal Mach Intell 2017;39(12):2481–95.
[16] Emerson Monica J, Jespersen Kristine M, Dahl Anders B, Conradsen Knut, Mikkelsen Lars P. Individual fibre segmentation from 3D X-ray computed tomography for characterising the fibre orientation in unidirectional composite materials. Compos A Appl Sci Manuf 2017;97:83–92.
[17] Ioffe S, Szegedy C. Batch Normalization: Accelerating Deep Network Training by Reducing Internal Covariate Shift.2015:448-56.
[18] Jia Y, Shelhamer E, Donahue J, Karayev S, Caffe Darrell T. Convolutional architecture for fast feature embedding. Acm International Conference on Multimedia, 2014.
[19] He K, Zhang X, Ren S, Sun J. Delving deep into rectifiers:Surpassing human-level performance on imagenet classification. In: ICCV 2015.
[20] Kingma D, Adam BaJ. A method for stochastic optimization. Comput Sci 2014.
[21] Lorensen WE, Cline HE. Marching cubes: a high resolution 3D surface construction algorithm. Acm Siggraph Comput Graphics 1987;21(4):163–9.
[22] Garland M, Heckbert PS. Surface simplification using quadric error metrics.ACM SIGGRAPH. Computer Graphics. 1997;1997:209–16.
[23] Blacklock M, Hayhurst DR. Initial elastic properties of unidirectional ceramic matrix composite fiber tows. J Appl Mech 2012;79(5).
[24] Y. J. Xu WHZA. Prediction of effective elastic modulus of plain weave multiphase and multilayer silicon carbide ceramic matrix composite. MATER SCI TECH-LOND.2008;24(4):435-42.
[25] Fouard C, Malandain G, Prohaska S, Westerhoff M. Blockwise processing applied to brain microvascular network study. IEEE Trans Med Imaging 2006;25 (10):1319–28.
[26] Naouar N, Vidal-Sallé E, Schneider J, Maire E, Boisse P. Meso-scale FE analyses of textile composite reinforcement deformation based on X-ray computed tomography. Compos Struct 2014;116:165–76.
[27] Otsu N. A threshold selection method from gray-level histograms. IEEE Trans Syst Man Cybernet 1979;9(1):62–6.
[28] Bénézech J, Couégnat G. Variational segmentation of textile composite preforms from X-ray computed tomography. Compos Struct 2019;230:111496.
[29] Huang W, Causse P, Brailovski V, Hu H, Trochu F. Reconstruction of mesostructural material twin models of engineering textiles based on Micro-CT Aided Geometric Modeling. Compos A Appl Sci Manuf 2019;124:105481.
[30] Liu X, Zhang D, Sun J, Yu S, Dai Y, Zhang Z, et al. Refine reconstruction and verification of meso-scale modeling of three-dimensional five-directional braided composites from X-ray computed tomography data. Compos Struct 2020;245:112347.